Nano-Micro Letters

ISSN 2311-6706
e-ISSN 2150-5551
CN 31-2103/TB

ARTICLE

https://doi.org/10.1007/s40820-019-0354-1

Cite as
Nano-Micro Lett.
(2020) 12:18

Received: 24 October 2019
Accepted: 3 December 2019

Highly Efficient Photoelectrocatalytic Reduction of CO_2 to Methanol by a p–n Heterojunction CeO_2/CuO/Cu Catalyst

Zhengbin Pan[1,2], Ershuan Han[1,2], Jingui Zheng[2], Jing Lu[2], Xiaolin Wang[2], Yanbin Yin[2], Geoffrey I. N. Waterhouse[2,3] ✉, Xiuguo Wang[1] ✉, Peiqiang Li[2] ✉

Zhengbin Pan and Ershuan Han have contributed equally to this work.

✉ Geoffrey I. N. Waterhouse, g.waterhouse@auckland.ac.nz; Xiuguo Wang, wangxiuguo@caas.cn; Peiqiang Li, chem_carbon@outlook.com

[1] Tobacco Research Institute of Chinese Academy of Agricultural Sciences (CAAS), Qingdao 266101, People's Republic of China

[2] College of Chemistry and Material Science, Shandong Agricultural University, Tai'an, 271018, People's Republic of China

[3] School of Chemical Sciences, The University of Auckland, Auckland 1142, New Zealand

HIGHLIGHTS

- Flower-like CeO_2 nanoparticles enhance the performance of CuO nanoparticle/Cu.
- The system benefits from the heterojunction between p-type CuO and n-type CeO_2.
- The selective reduction of CO_2 to methanol on the target catalyst is studied.

ABSTRACT Photoelectrocatalytic reduction of CO_2 to fuels has great potential for reducing anthropogenic CO_2 emissions and also lessening our dependence on fossil fuel energy. Herein, we report the successful development of a novel photoelectrocatalytic catalyst for the selective reduction of CO_2 to methanol, comprising a copper catalyst modified with flower-like cerium oxide nanoparticles (CeO_2 NPs) (a n-type semiconductor) and copper oxide nanoparticles (CuO NPs) (a p-type semiconductor). At an applied potential of − 1.0 V (vs SCE) under visible light irradiation, the CeO_2 NPs/CuO NPs/Cu catalyst yielded methanol at a rate of 3.44 μmol cm^{-2} h^{-1}, which was approximately five times higher than that of a CuO NPs/Cu catalyst (0.67 μmol cm^{-2} h^{-1}). The carrier concentration increased by ~ 10^8 times when the flower-like CeO_2 NPs were deposited on the CuO NPs/Cu catalyst, due to synergistic transfer of photoexcited electrons from the conduction band of CuO to that of CeO_2, which enhanced both photocatalytic and photoelectrocatalytic CO_2 reduction on the CeO_2 NPs. The facile migration of photoexcited electrons and holes across the p–n heterojunction that formed between the CeO_2 and CuO components was thus critical to excellent light-induced CO_2 reduction properties of the CeO_2 NPs/CuO NPs/Cu catalyst. Results encourage the wider application of composite semiconductor electrodes in carbon dioxide reduction.

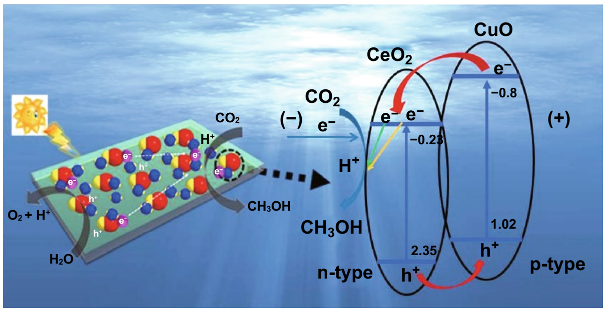

KEYWORDS CO_2 reduction; Photoelectrocatalysis; p–n heterojunction; Cerium oxide; Copper oxide

1 Introduction

Since the beginning of the industrial revolution in the late 1700s, humans have heavily relied on cheap and abundant fossil fuels as an energy source. Indeed, modern societies are still very heavily reliant on fossil fuels for energy and as a feedstock for the manufacture of commodity chemicals. However, fossil fuels are a non-renewable energy source, meaning that they will likely be exhausted over the next few hundred years, motivating the development alternative renewable energy technologies (especially solar and wind) as a means of achieving energy supply security. A further downside of using fossil fuels for energy is the associated CO_2 emissions, which directly promote global warming via the greenhouse effect [1–4]. However, if viewed from another perspective, the CO_2 produced via combustion of fossil fuels or biomass sources represents a cheap C_1 building block (i.e., a resource to be exploited rather than an annoying waste product) [5, 6]. Accordingly, over the past decade, and enormous amount of research effort has been directed toward the development of efficient technologies for converting CO_2 into valuable chemical and fuels via processes such as catalytic hydrogenation [7, 8], photocatalytic (PC) reduction [9, 10], electrocatalytic (EC) reduction [11, 12], photoelectrocatalytic (PEC) reduction [13, 14], and biotransformation to solve environmental and energy issues [15, 16]. Among these, EC, PC, and PEC are perhaps the three most promising approaches for future large scale CO_2 reduction. In EC, CO_2 is reduced via the transfer of electrons and also protons to CO_2, though most metal electrodes suffer from high overpotentials for CO_2 reduction, and thus produce large amounts of H_2 along with any products of CO_2 reduction (i.e., the electrodes generally have poor selectivity for CO_2 reduction) [17, 18]. In CO_2 reduction by semiconductor photocatalysis, light irradiation causes electrons to be promoted from the semiconductor valence band into the conduction band (CB), thus giving rise to charge carriers capable of reducing CO_2 to CO and other products when the semiconductors valence band (VB) and CB are suitably positioned relative to the redox processes needed for CO_2 reduction and typically water oxidation, respectively [19]. However, the efficiency and performance of most photocatalysts for CO_2 reduction are limited by bulk recombination of photoexcited electrons and holes. In this context, PEC is a particularly promising method for CO_2 reduction, wherein an applied potential is used to prevent the bulk recombination of bulk photoelectrons and holes, thereby increasing the availability of photoexcited electrons for reaction with CO_2. Various semiconductors have been studied in relation to PC and PEC CO_2 reduction. In order to maximize solar spectrum utilization, it is desirable to use a semiconductor with a narrow band gap that absorbs in the visible regime [20]. However, the narrower the band gap, the more rapid the electron–hole pair recombination, and hence many narrow band gap semiconductors show poor PC efficiencies for CO_2 reduction. Thus, PEC systems are generally preferred, with various approaches being adopted to enhance the conversion efficiency of PEC catalysts for CO_2 reduction including the introduction of co-catalysts [21, 22], bulk doping of the semiconductor with metal cations to increase the light absorption range and/or to introduce electron traps [23, 24], p–n junction construction [25], among others. Furthermore, by nanostructuring semiconductor PC or by creating hierarchical semiconductor arrays, materials with large specific surface areas and abundant active sites for adsorbing CO_2 can be created, thereby facilitating CO_2 reduction under direct sunlight or simulated sunlight [26].

Copper oxide-based semiconductors have received much attention in relation to the catalytic reduction CO_2. CuO has excellent EC activity for CO_2 reduction, exhibiting very high selectivity to CH_3OH [27, 28]. Further, Gusain et al. [29] demonstrated that reduced graphene oxide–copper oxide nanocomposites were able to convert CO_2 to CH_3OH photocatalytically under visible light irradiation. Kim et al. [30] developed a highly efficient p–n–p $Cu_2O/S\text{-}TiO_2/CuO$ heterojunction for the photocatalytic conversion of CO_2 to CH_4. Although CuO can readily be photoexcited using visible light, rapid recombination of photogenerated electrons and holes limits its photocatalytic activity [31]. Combining CuO with other semiconductors through heterojunction is effective in suppressing electron–hole pair recombination, offering a pathway to greatly improve the PC performance of CuO. Other strategies for suppressing electron–hole pair recombination include the addition of suitable co-catalysts or photosensitizers that can supply electrons or remove holes effectively from CuO, or alternatively enhance the absorption incoming visible light [32]. CeO_2 is an inexpensive rare earth semiconductor that finds widespread use in solar cells, optical devices, sensors, and sunscreen materials [33, 34]. It is also widely used in catalysis as a support due to its outstanding oxygen storage behavior, which arises from valence change switching

https://doi.org/10.1007/s40820-019-0354-1

between Ce^{3+} and Ce^{4+} [35, 36]. Considering the relative positions of the conduction and valance bands of n-type CeO_2 and p-type CuO, we hypothesized that the construction of a CeO_2/CuO heterojunction should be highly beneficial for improving the PC and PEC performance for CO_2 reduction. Under light irradiation, electrons photoexcited into the CB of CuO would be transferred into the CB of CeO_2, whereas holes (h^+) created in the VB of CeO_2 under light irradiation would migrate into the VB of CuO. Via such exchange of electrons holes between CuO and CeO_2, more charge carriers should be available to drive CO_2 reduction to methanol (the dominant product for CO_2 reduction over CuO-based catalysts). To date, very little work has been done relating to the application of CeO_2/CuO heterojunctions in solar-driven CO_2 reduction to fuels, motivating a detailed investigation.

Herein, we systematically explored the performance of a CeO_2/CuO/Cu catalyst system for PEC CO_2 reduction under visible light. Flower-like n-type CeO_2 nanoparticles were grown on a p-type CuO NPs/Cu foil catalyst by electrodeposition, with the resulting heterojunction catalyst (denoted herein as CeO_2 NPs/CuO NPs) then being subjected to detailed physicochemical and electrochemical characterization, along with PEC CO_2 reduction tests in a CO_2-saturated aqueous $KHCO_3$ solution. The overarching aim of the research was to establish whether CeO_2 addition could significantly enhance the PEC performance of CuO-based catalyst for reduction CO_2 to CH_3OH.

2 Experimental Section

2.1 Preparation of the CuO NPs Catalyst

All reagents were supplied by Aladdin Reagent Co., Ltd. A pure copper foil (99.99% Cu, $50 \times 20 \times 1$ mm^3) was polished with coarse sandpaper, then metallographic sandpaper, to achieve a mirror finish. The polished Cu foil was washed repeatedly with anhydrous ethanol and then air-dried. The Cu foil was then anodized in an ethylene glycol–water solution (volume ratio 97:3) containing 0.25wt% NH_4F. A polished Ti foil (99.99% Ti, $50 \times 20 \times 1$ mm^3) was used as the cathode. The separation between the anode and cathode was 1 cm, and the temperature of electrolyte maintained at 20 °C. Under magnetic stirring, CuO NPs were formed by holding the Cu foil electrode at a potential of 30 V for 1.5 h. The prepared electrode was then washed with distilled water before being heated from room temperature to 300 °C in a tube furnace under O_2. The catalyst was held at 300 °C for 3 h and then cooled to 20 °C at a rate of 1 °C min^{-1} [13]. The obtained catalyst is denoted herein as CuO NPs.

2.2 Preparation of the Flower-like CeO_2 NPs/CuO NPs Composite Catalyst

Flower-like CeO_2 NPs were subsequently deposited on the CuO NPs catalyst via an electrochemical method that used a three-electrode system, comprising the CuO NPs catalyst as the working electrode, a Pt wire as the counter electrode and a saturated calomel electrode (SCE) as the reference electrode. The flower-like CeO_2 NPs were introduced by electrodeposition at a constant current density of 2 mA cm^{-2} for 2 h. An aqueous electrolyte containing 10 mM $Ce(NO_3)_3 \cdot 6H_2O$, 50 mM KCl, and 50 mM NH_4Cl, with the electrolyte temperature maintained at 70 °C [37]. The obtained catalyst, denoted herein as the flower-like CeO_2 NPs/CuO NPs, was washed with distilled water and air-dried at room temperature.

2.3 Catalysts Characterization

The surface morphologies of the catalysts were examined using scanning electron microscopy (SEM, Hitachi SU8010). The particle size was calculated by the Nano Measurer 1.2 software. The microscope was operated at an acceleration voltage of 5.0 kV for the imaging. High-resolution transmission electron microscopy (HRTEM) analyses were performed on a JEM-2100 microscope operating at 200 kV. The crystal structure of the samples was probed by X-ray diffraction (XRD) on a Rigaku D/MAX-rA diffractometer (Japan) equipped with a Cu-Kα source ($\lambda = 0.154178$ nm,). X-ray photoelectron spectroscopy (XPS) measurements were performed on a ESCALAB 250 equipped with a monochromatic Al Kα source ($h\nu = 1486.7$ eV). UV–visible diffuse reflectance spectra (UV–Vis DRS) were collected on a UV–Vis spectrophotometer (TU-1901. Beijing Purkinje General Instrument Co., Ltd.), and the wavelength ranged from 400 to 700 nm. Dielectric constants were measured at room temperature using a TH2826 LCR digital bridge (Shanghai Double Asa Electronics Co., Ltd.) operating at 2 MHz. The electrochemical properties of the catalysts were evaluated using a CHI660D potentiostat (Shanghai Chenhua Instrument Co., Ltd.).

2.4 Photoelectrocatalytic CO_2 Reduction Experiments

PEC CO_2 reduction experiments were conducted in a quartz reaction cell containing a three-electrode array comprising the CeO_2 NPs/CuO NPs composite catalyst as the working electrode, a Pt plate as the counter electrode and a saturated calomel electrode (SCE) as the reference electrode. The cell was interfaced with a CHI660D potentiostat and a circulating water device to maintain a constant temperature of 25 °C. Scheme 1 shows a schematic of the PEC cell used for reduction CO_2 reduction. The cathode electrolyte was aqueous 0.1 mol L^{-1} $KHCO_3$ (40 mL), with CO_2 gas bubbled through the cathode electrolyte at a rate of 40 mL min^{-1} during the reaction. In fresh form of 0.1 mol L^{-1} $KHCO_3$, it has pH (8.34), but the reaction is carried out under CO_2, so pH change to 6.8. The LSV is affected by different pH, experiments have been done under pH = 7.0 and pH = 9.0, and the impact was also calculated, which is 0.12%. So the proton reduction has almost no impact on the experimental conclusion [38]. A 500-W xenon lamp ($420 \le \lambda \le 800$ nm, 100 mW cm^{-2}) was used for the PEC CO_2 reduction tests, which were performed over a testing period of 6 h. The qualitative and quantitative analysis of products was performed by gas chromatography. The gas chromatograph (GC-9A, Shimadzu) was equipped with an air pump and hydrogen generator, FID and TCD detectors, and a Porapak Q (80–100) glass packed column. The column temperature was maintained at 180 °C and the detector temperature at 200 °C. The carrier gas used was high purity N_2 (flow rate 30 mL min^{-1}).

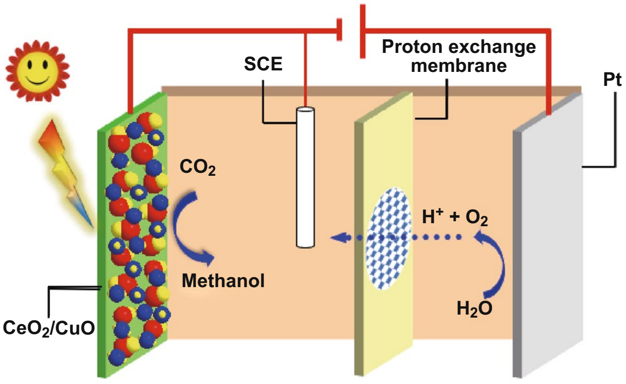

Scheme 1 The PEC cell for CO_2 reduction

3 Results and Discussion

3.1 Characteristics of the CuO NPs and CeO_2 NPs/CuO NPs Catalysts

The surface morphologies and structural properties of the CuO NPs and CeO_2 NPs/CuO NPs catalysts were examined by SEM, TEM, and XRD, with data for these electrodes being summarized in Fig. 1. As shown in Fig. 1a, anodizing the surface of the Cu foil was effective in covering the surface of the foil with CuO NPs. The CuO NPs were pseudo-spherical and relatively uniform in size, with the average size around 180 nm (Fig. 1a_2). XRD results confirmed the formation of CuO NPs (Fig. 1c). Flower-like CeO_2 NPs were grown on the CuO NPs catalyst by electrodeposition (Fig. 1b). The flower-like CeO_2 NPs morphology with thin petals was expected to be near ideal for promoting PEC CO_2 reduction on the hybrid heterojunction catalyst, offering a very large specific surface area for CO_2 adsorption and reduction (Fig. S1). XRD results further confirmed the successful growth of nanocrystalline CeO_2 on the CuO NPs catalyst (Fig. 1c). Diffraction peaks appearing at $2\theta = 28.58$, 33.13, 47.56, and 56.43 could readily be assigned to the (111), (200), (220), and (311) reflections of CeO_2 (JCPDS No. 65-5923). In addition, a small amount of Ce_2O_3 was detected, implying that the modified electrode contained an abundance of Ce^{3+}/Ce^{4+} species and thus likely strong oxygen storage capacity [39]. The structure of the flower-like CeO_2 NPs was examined further using HRTEM. Figure 1d shows that the sample was composed of CeO_2 nanocrystals. The inset in Fig. 1d shows lattice fringes with spacings of 0.31, 0.19, and 0.27 nm, corresponding to the interlayer distance between the (111), (220), and (200) lattice planes, respectively, of cubic CeO_2 [40]. These results are consistent with the XRD findings (Fig. S2). Previous studies have shown the CeO_2 (111) plane to be very important for PC applications, as it is thermodynamically stable and very sensitive to light [35, 36].

The visible light absorption characteristics of the as-prepared CuO NPs and flower-like CeO_2 NPs/CuO NPs catalysts were examined by UV–Vis DRS (Fig. 2a). The flower-like CeO_2 NPs/CuO NPs catalyst exhibited absorption across the visible region than CuO NPs catalyst, as expected since nanocrystalline CeO_2 is optically active at visible wavelengths (a pale yellow color). Band gaps (E_g)

https://doi.org/10.1007/s40820-019-0354-1

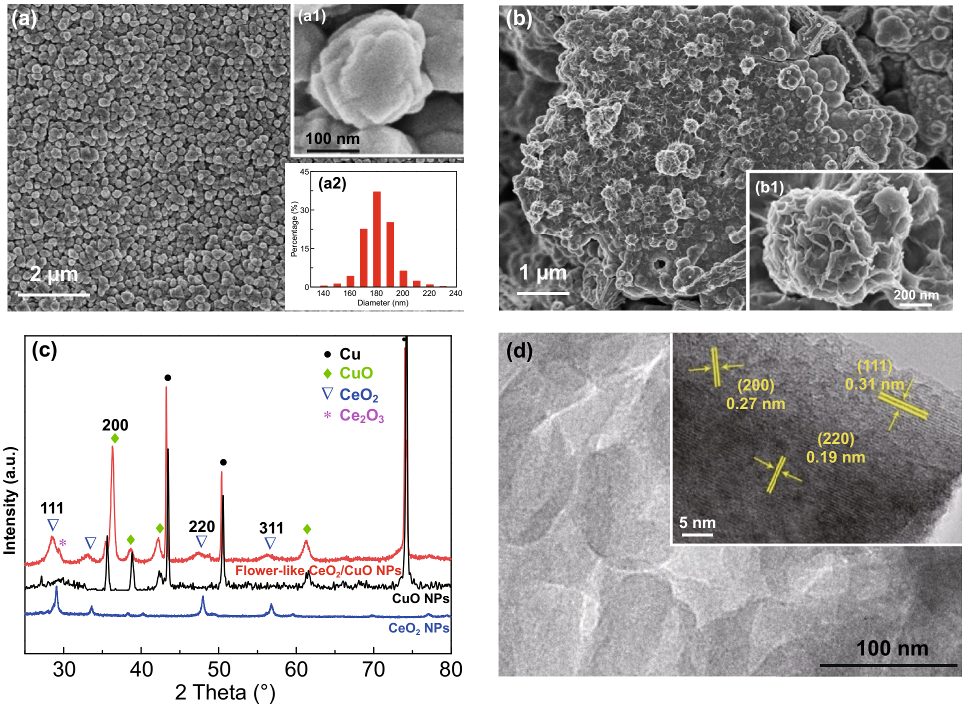

Fig. 1 SEM images of CuO NPs at **a** low magnification and $\mathbf{a_1}$ high magnification. $\mathbf{a_2}$ Particle size distribution for CuO NPs. SEM images for flower-like CeO_2 NPs at **b** low magnification and $\mathbf{b_1}$ high magnification. **c** XRD patterns for CuO NPs and flower-like CeO_2 NPs/CuO NPs. **d** HRTEM image of CeO_2 NPs. The inset shows a high magnification image, revealing lattice fringes characteristic for CeO_2

for the different electrodes were estimated using the Tauc equation (Eq. 1) [41]:

$$\alpha hv = A(hv - E_g)^n \tag{1}$$

here α is the reciprocal of the absorption length, hv is the photon energy, and A is a constant. For direct band gap transitions, the index $n = 0.5$ and for indirect band gap transition $n = 2$. The band gap of the CuO NPs catalyst was calculated by applying a linear fit to a plot of $(\alpha hv)^{0.5}$ and hv experimental curves, with the analysis yielding an E_g of 1.82 eV (Fig. 2b). This value is in good accord with prior literature reports for CuO [32]. For the flower-like CeO_2 NPs/CuO NPs catalyst, the estimated E_g value was 2.10 eV (Fig. 2c), representing the weighted sum of the band gap values of CuO and CeO_2. The data in Fig. 2 confirm that both electrodes showed a good optical response at visible wavelengths, as required for visible light-driven PC and PEC processes.

When a semiconductor is in contact with an electrolyte, a space charge layer will be formed in the semiconductor surface due to the difference in Fermi level between the bulk and the surface (resulting in band bending), while a Helmholtz layer will be formed on the electrolyte side of the semiconductor/electrolyte interface. For such a system where a semiconductor is in contact with an electrolyte, a capacitance (C) results through coupling of the space charge layer capacitance (C_{sc}) in series with the solution Helmholtz layer capacitance (C_H) (note: C_H is usually negligible relative to C_{sc}). Changing the polarization potential (E) of a semiconductor can change the space charge layer capacitance of the semiconductor, which can be described by the Mott–Schottky equation (Eq. 2) [42]:

$$\frac{1}{C_{SC}^2} = \frac{2}{\varepsilon_0 \varepsilon_r N_A A^2}\left(E - E_{fb} - \frac{kT}{e}\right) \tag{2}$$

here C_{sc}, N_A, ε_0, A, ε_r, E, k, T, E_{fb} and e are the space charge layer capacitance, doping concentration, vacuum dielectric constant, the contact area between the electrode and the solution, dielectric constant of the semiconductor, polarization potential, the Boltzmann constant, absolute temperature, the flat band potential, and the electric charge, respectively. By plotting C_{sc} versus the polarization voltage E, a straight-line section is obtained. Extending the tangent to that straight-line section to the polarization voltage axis yields obtain the flat band potential E_{fb} of a material. Figures 2d and S3 show Mott–Schottky plots for the flower-like CeO_2 NPs/CuO

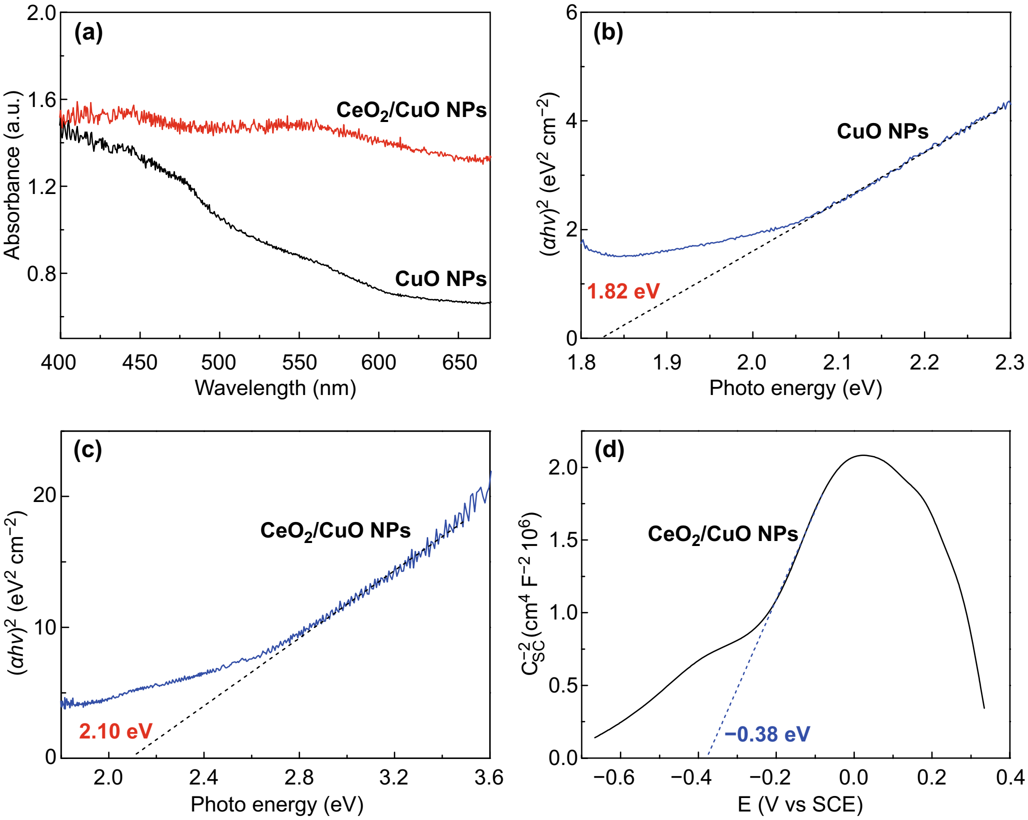

Fig. 2 **a** UV–Vis absorbance spectra for CuO NPs and flower-like CeO_2 NPs/CuO NPs. Tauc plots for **b** CuO NPs and **c** flower-like CeO_2 NPs/CuO NPs. **d** Mott–Schottky plots for flower-like CeO_2 NPs/CuO NPs

NPs catalyst and CuO NPs catalyst, respectively. The slope of the first half is positive, while the slope of the second half is negative, it shows p–n semiconductor characteristics after the CeO_2 NPs deposited on the CuO NPs (Fig. 2d). E_{fb} of CuO NPs and CeO_2 NPs/CuO NPs estimated from the plots were 0.82 eV (Fig. S3) and − 0.38 eV (Fig. 2d), respectively. The valence band maximum (VBM) of p-type semiconductor is approximately located at 0.2 eV below the flat band potential, so the VB of the CuO NPs is located at 1.02 eV [43]. Taking the fermi level for each electrode and using the Mott–Schottky equation, the acceptor concentrations (N_A) for the CuO NPs catalyst and flower-like CeO_2 NPs/CuO NPs catalyst were calculated to be 3.47×10^{-5} and 2.93×10^4 m^{-3}, respectively. The carrier concentration for the flower-like CeO_2 NPs/CuO NPs catalysts was thus a remarkable 10^8 times higher than that of the CuO NPs electrode. These data provide convincing evidence that the decoration of the CuO NPs catalyst with flower-like CeO_2 NPs was effective in enhancing the separation of photogenerated electrons and holes. To explain this, the intrinsic properties of CuO (p-type conductor) and CeO_2 (n-type conductor) need to be considered. On electrodepositing CeO_2 onto the CuO NPs catalyst, p–n heterojunctions are formed at the interface between the two components (Fig. 2d). The experimental data suggest that when an external voltage is applied, the internal charge within the heterojunction actually opposed the applied external voltage, thus increasing the conductivity in the interfacial region [44–46]. Thus, creation of p–n heterojunctions is highly advantageous for promoting interfacial charge transfer and enhancing charge carrier mobilities [47]. Under the conditions used in the PEC CO_2 reduction tests below, a negative voltage (− 1.0 V) was used, in which case the net flow of electrons will be from CuO to CeO_2 (as depicted in Scheme 2), with CeO_2 acting as the adsorption and reduction site for CO_2.

In order to further probe the excellent properties of the flower-like CeO_2 NPs/CuO NPs system, XPS was applied to examine the chemical speciation of Cu, O, and Ce in the electrode. Figure 3a shows the Cu 2p XPS spectrum of the catalyst. The spectrum shows a set of peaks in a 2:1 area ratio (readily assigned to Cu $p_{3/2}$ and Cu $2p_{1/2}$ signals, respectively), along with a corresponding shake-up satellites at higher binding energies, indicating the presence of Cu^{2+} (3 d^9). The binding energy of the Cu

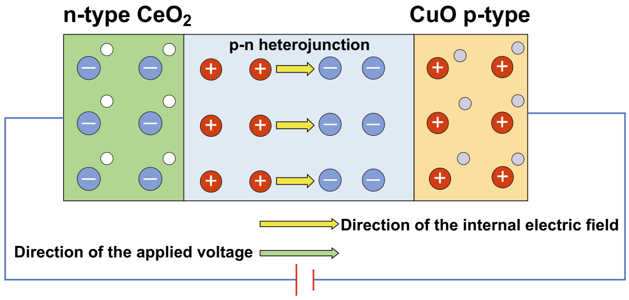

Scheme 2 Charge separation under an applied the voltage in the p–n junction flower-like CeO_2 NPs/CuO NPs system

$2p_{3/2}$ peak at 933.8 eV is also consistent with Cu^{2+} in CuO. The O 1 s peak at 529.8 eV (Fig. 3b) contains unresolved contributions from CuO (529.6 eV) and CeO_2 (529.2 eV). The Ce 3d spectrum (Fig. 3c) showed a multitude of peaks, which could be assigned to Ce^{4+} and Ce^{3+} species following the description by Burroughs et al. [48] wherein *v* and *u* represent different $3d_{5/2}$ and $3d_{3/2}$ states, respectively. The characteristic peaks of Ce^{4+} are labeled *v, v”, v”‘, u, u”* and *u*”‘. The peaks labeled *v*’ and *u*’ are associated with Ce^{3+} ($3d_{5/2}$ and $3d_{3/2}$, respectively), indicating the presence of oxygen vacancies on the surface of the CeO_2 [49]. The percentage of Ce^{3+} in the flower-like CeO_2 NPs/CuO NPs system was estimated to be around 34.82%, with the balance being Ce^{4+}. The valence of Ce is analyzed in Table 1, and the result is consistent with the CeO_2 existing in the form of CeO_{2-x}.

Based on the aforementioned experimental studies of the flower-like CeO_2 NPs/CuO NPs catalyst, mechanisms can be proposed for charge separation and thus CO_2 reduction under EC, PC, and PEC regimes. On forming a CeO_2/CuO heterojunction, an internal electric field will form at the interface between n-type CeO_2 and p-type CuO, which inhibit the transfer of carriers between the two semiconductors.

If an external voltage is applied (under EC conditions as shown in Scheme 2) in the same direction as the internal electric field, the internal electric field should have become larger, and the conductivity poorer. However, we found that the internal electrical field of the CeO_2 NP/CuO NPs was actually opposed to the external voltage (Scheme 2), increasing the interfacial conductivity, resulting in electron transfer to the CeO_2 component. Accordingly, in the presence of CO_2, rapid reduction to methanol on CeO_2 will occur aided by protons coming from the anode (see CO_2 tests below).

Under light irradiation (no voltage applied, i.e., the PC regime, Scheme 3a), electrons will be photoexcited from the VB to the CB of both CuO and CeO_2. Electrons photoexcited in CuO will be transferred to CeO_2 since the CB of CeO_2 (− 0.23 eV) is more positive than that of the CuO (− 0.80 eV) [50]. Conversely, holes created in the VB of CeO_2 will migrate into the VB of CuO. It results in the suppression of electron–hole pair recombination and an increase in the availability of electrons for reducing CO_2 on the CeO_2 nanoparticles.

When light and electricity are applied simultaneously (Scheme 3b), the concentration of electrons reaching CeO_2 will be further enhanced through the coupling of processes described in Scheme 2 and 3a. Accordingly, PEC CO_2 reduction, which synergistically combines the advantages of EC and PC systems, was expected to offer the best performance for CO_2 reduction to CH_3OH, which was confirmed by the experiment below.

The instantaneous photocurrent density excited by visible light provides a useful indication of the efficiency of the separation of photogenerated electrons and holes on the surface of a semiconductor photocatalyst. The higher the instantaneous photocurrent density, the more sensitive the

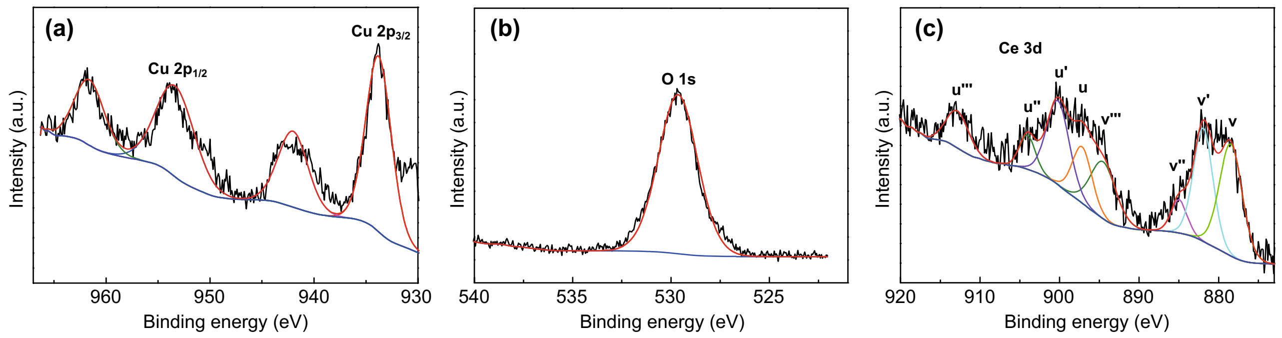

Fig. 3 XPS characterization of the flower-like CeO_2 NPs/CuO NPs composite catalyst. **a** Cu 2p region, **b** O 1s region, and **c** Ce 3d region

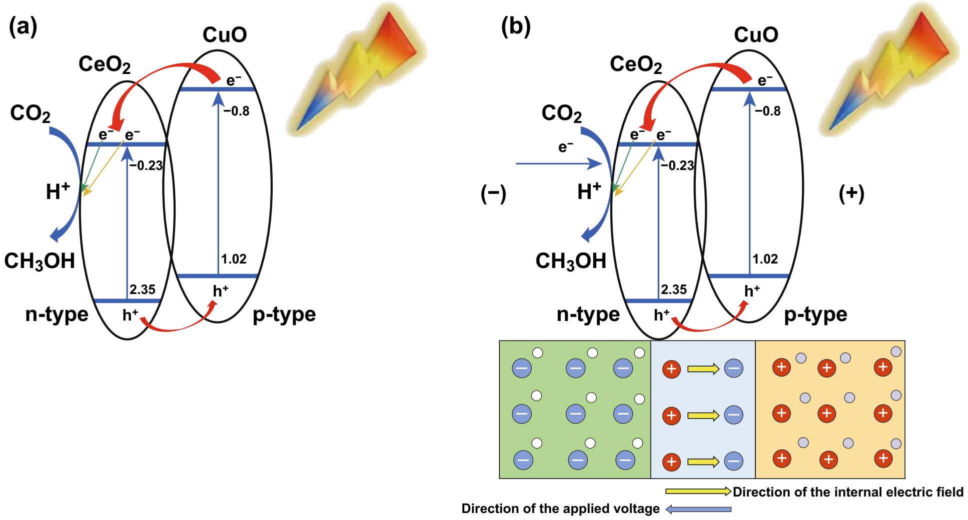

Scheme 3 Proposed mechanisms for **a** PC CO_2 reduction, and **b** PEC CO_2 reduction on the flower-like CeO_2 NPs/CuO NPs composite catalyst. The mechanism of EC CO_2 reduction is shown in Scheme 2

photocatalyst is to visible light and the greater the separation of photogenerated electrons and holes. Figure 4a shows instantaneous photocurrent density changes for the CuO NPs and CeO_2 NPs/CuO NPs catalysts over several light-on and light-off cycles of visible light irradiation. For both electrodes, the photocurrent density increased rapidly when irradiated with visible light and then dropped sharply when the light was turned off. Importantly, the photocurrent density of the flower-like CeO_2 NPs/CuO NPs catalyst (40.75 μA cm^{-2}) was about 10 times higher than that of the CuO NPs catalyst (4.28 μA cm^{-2}) under visible light irradiation, indicating that charge separation much more effective on the CeO_2 NPs/CuO NPs. This data provides further evidence that CeO_2/CuO heterojunction construction was effective in enhancing the light absorbing and availability of electrons and holes for photoreactions (by effectively facilitating charge separation). Further, the photocurrent density of CeO_2 NPs/CuO NPs electrode appeared to be quite stable over the three on–off cycles, suggesting that the electrode had stable performance.

The XPS valence band spectrum for the flower-like CeO_2 NPs/CuO NPs catalyst is shown in Fig. 4b. The spectrum could be fitted using two peaks at 3.97 and 5.39 eV, corresponding to valence oxygen states CeO_2 and CuO. The position of the VBM was obtained directly from the spectrum using a linear extrapolation, yielding a VBM of 1.47 eV.

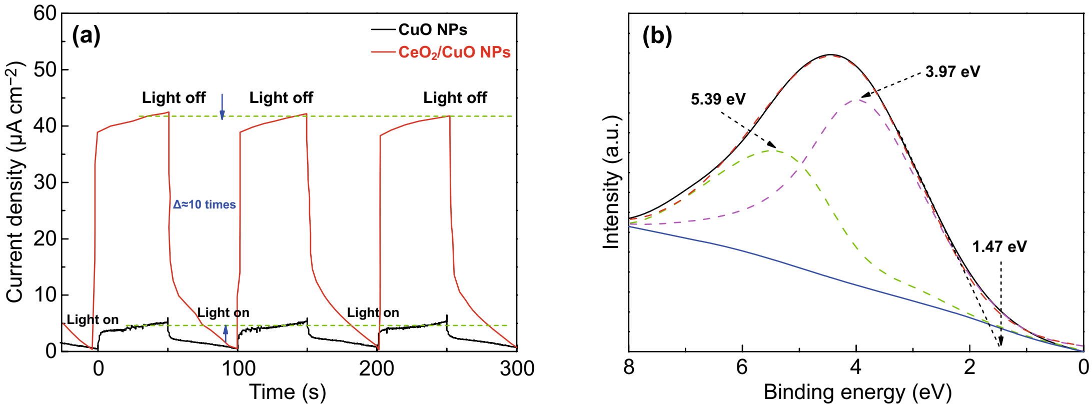

Fig. 4 **a** Instantaneous photocurrent density of catalyst, **b** VB photoemission spectrum (solid line) and Gaussian fit (dashed line) of catalyst

Since the band gap of the flower-like CeO_2 NPs/CuO NPs catalyst was estimated to be around 2.10 eV (Fig. 2c), the CB position of CeO_2 NPs/CuO NPs catalyst was thus around − 0.63 eV.

3.2 Photoelectrocatalytic Reduction of CO_2

Having characterized the CuO/NPs and flower-like CeO_2 NPs/CuO NPs catalyst in detail, we then examined the performance of these two electrodes for PEC reduction CO_2. Figure 5a shows linear sweep voltammetry (LSV) curves for each electrode in a 0.1 mol L^{-1} $KHCO_3$ solution, under N_2 or CO_2 purging. In each case, the increase in the current observed as the potential is made more negative is due to the reduction of water and/or the catalytic reduction of CO_2. The current response of the CeO_2 NPs/CuO NPs catalyst increased under light irradiation, under both a N_2 purge (cf. curves in Fig. 5a_2, a_3) and a CO_2 purge (cf. curves in Fig. 5a_4, a_5). Results indicate that the CeO_2 NPs/CuO NPs catalyst had good performance for PEC CO_2 reduction. Further, the PEC CO_2 reduction performance of the CeO_2 NPs/CuO NPs catalyst was much better than that of the CuO NPs catalyst under light irradiation and with a CO_2 purge (cf. curves in Fig. 5a_5, a_1). And then the net current density ($i_{CO_2} - i_{N_2}$) of the CeO_2 NPs/CuO NPs with light and without light was compared (Fig. S4), the current density of light is much higher than dark one. It is more validated that the CeO_2 NPs/CuO NPs have more excellent ability for PEC reduction CO_2. The photoelectric conversion efficiencies of the flower-like CeO_2 NPs/CuO NPs and CuO NPs catalysts are shown in Fig. 5b. The CO_2 to CH_3OH conversion efficiency on the CuO NPs/electrode at the applied potential of − 1.0 V (vs SCE) was only 5.98%, whereas the efficiency for the same conversion on the CeO_2 NPs/CuO NPs catalyst was 55.64% (i.e., around nine times higher).

The products of PEC CO_2 reduction on the CeO_2 NPs/CuO NPs catalyst were analyzed by gas chromatography. At externally applied bias voltages ranging from − 0.8 to − 1.2 V, the only carbon-containing reduction product detected was methanol. Figure 5c shows the methanol yield over the CeO_2 NPs/CuO NPs catalyst at different applied potentials. As the applied voltage was increased up to

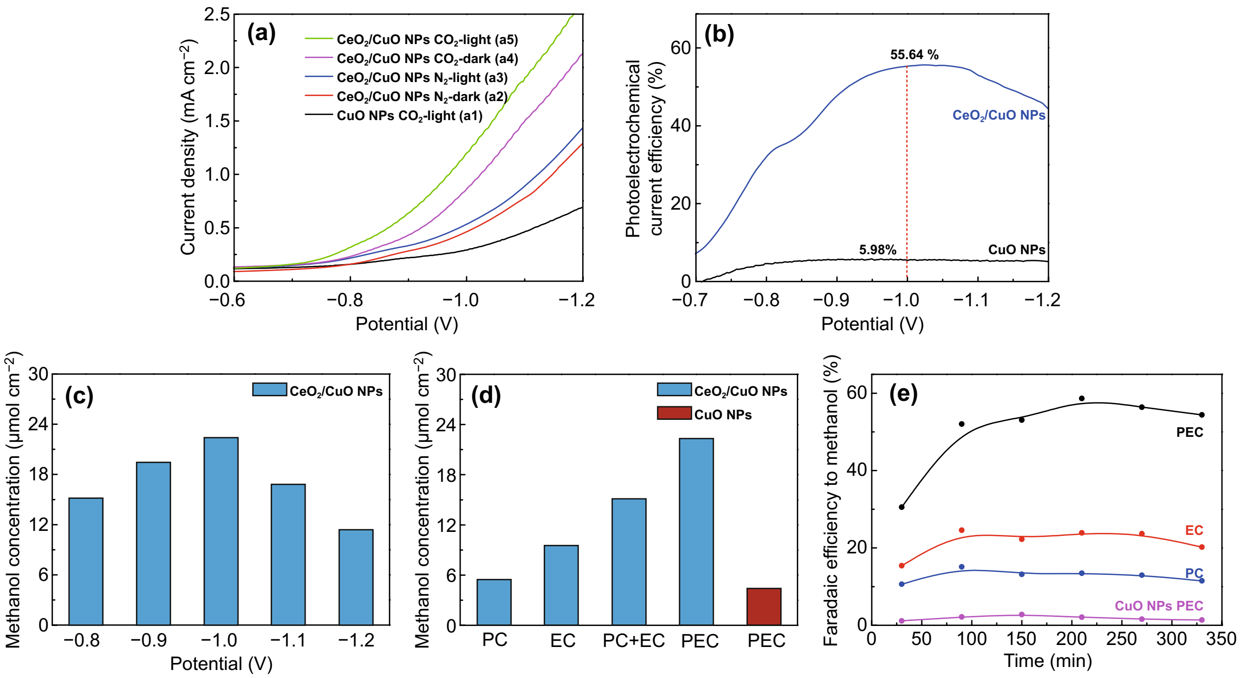

Fig. 5 **a** Linear sweep voltammetry curves for different electrodes under light illumination and in the dark. The data were collected in a 0.1 mol L^{-1} $KHCO_3$ solution, under N_2 or CO_2 purging. **b** Photoelectric conversion efficiencies for different electrodes. **c** The methanol concentration at different potentials following 6.5 h of light illumination for the CeO_2 NPs/CuO NPs catalyst. **d** The methanol concentration after 6.5 h for PEC, EC, and PC reduction of CO_2 at − 1.0 V. **e** Faradaic efficiency for CO_2 reduction to methanol under PEC, EC, and PC conditions at − 1.0 V

− 1.0 V, the yield of methanol increased, reaching 22.32 μmol cm^{-2} at − 1.0 V over 6.5 h (corresponding to a methanol production rate of 3.43 μmol cm^{-2} h^{-1}). As the potentials continued to increase, at higher potentials, the yield of methanol decreased. Results suggest that in the potential range from − 0.8 to − 1.0 V, the catalytic reduction of CO_2 is the dominant reaction occurring on the electrode. At more negative potentials, the hydrogen evolution reaction starts to compete with electrocatalytic CO_2 reduction.

Figure 5d shows comparison of the methanol yields for CO_2 reduction to methanol on the flower-like CeO_2 NPs/CuO NPs catalyst under PEC, EC, and PC regimes after 6.5 h of testing. Methanol yields decreased in the order PEC (22.32 μmol cm^{-2}) > EC (9.51 μmol cm^{-2}) > PC (5.53 μmol cm^{-2}). Thus, the methanol yield by PEC reduction of CO_2 was 2.35 and 4.04 times higher than the yields obtained by EC and PC. Further, the methanol yield by PEC on the CeO_2 NPs/CuO NPs catalyst (22.32 μmol cm^{-2}) was around 5 times higher than the methanol yield by PEC on the CuO NPs electrode (4.37 μmol cm^{-2}) for a reaction time of 6.5 h at a potential of − 1.0 V, indicated that CeO_2 addition greatly improved the PEC performance of the CeO_2 NPs/CuO NPs catalyst. The Faradaic efficiency for CO_2 reduction to methanol on the flower-like CeO_2 NPs/CuO NPs catalyst under different conditions (i.e., PEC, EC, and PC) in 0.1 mol L^{-1} $KHCO_3$ solution under a CO_2 purge is shown in Fig. 5e. The Faradaic efficiency for PEC was 58.67%, significantly higher than that realized by EC (24.57%) and PC (15.08%). Again, this reflects the action of both EC and PC processes under the PEC regime, which act cooperatively to increase the availability of electrons for CO_2 reduction. As expected, the PEC Faradaic efficiency of the CeO_2 NPs/CuO NPs catalyst for CO_2 reduction to CH_3OH at − 1.0 V was superior to that of the CuO NPs catalyst. Furthermore, the Faradaic efficiency of the CeO_2 NPs/CuO NPs catalyst remained ~ 55% at − 1.0 V over 6.5 h, implying that the heterojunction electrode had exceptional stability.

Considering all of the above, it can be concluded that the CeO_2 NPs/CuO NPs catalyst developed in this work demonstrated remarkable performance and stability for PEC CO_2 reduction to methanol. The electrode benefitted from the following synergies: (1) The direct electrodeposition of flower-like CeO_2 nanoparticles on the CuO NPs/Cu foil catalyst ensured intimate contact between the CeO_2 and CuO components, thus forming intimate p–n heterojunctions for electron transfer; (2) The flower-like CeO_2 offered an abundance of active sites for CO_2 adsorption and reduction, while also minimizing electron–hole pair recombination in CeO_2 under light irradiation due to the short electron transfer distance to the CeO_2 surface distance; (3) The combination of p-type CuO and n-type CeO_2 increased the carrier concentration in the CeO_2 NPs/CuO NPs catalyst by 10^8 times relative to the CuO NPs catalyst, which greatly enhanced CO_2 reduction performance; and (4) The CeO_2 NPs/CuO NPs catalyst possessed good optical absorption characteristics under visible light, with the photoexcitation of both CeO_2 and CuO, as well as electron transfer from CuO to CeO_2 (matched by hole migration from CeO_2 to CuO), generating an abundance of electrons at the CeO_2 surface for CO_2 reduction. Thus, when light and external voltage (− 1.0 V) were simultaneously applied to the CeO_2 NPs/CuO NPs catalyst in a 0.1 M $KHCO_3$ solution purged with CO_2, the reduction of CO_2 to CH_3OH occurred very efficiently evidenced by a Faradaic efficiency of almost 60% at − 1.0 V (using protons generated by water oxidation at the anode). Results encourage the development of p–n junction PEC systems for CO_2 reduction to oxygenate and fuels.

4 Conclusions

Electrodeposition of flower-like CeO_2 NPs significantly enhanced the performance of a CuO NPs/Cu catalyst for PEC CO_2 reduction to methanol under visible light irradiation. The system benefitted from the creation of intimate p–n heterojunctions between p-type CuO and n-type CeO_2. Under both an applied electric potential of − 1.0 V, or visible light irradiation, electrons migrated from CuO nanoparticles to the flower-like CeO_2 nanoparticles, resulting in an abundance of electrons on the surface of the CeO_2 nanoparticles for CO_2 reduction to methanol. Under visible light illumination, the yield of methanol for the CeO_2 NPs/CuO NPs/Cu catalyst at − 1.0 V in a CO_2–saturated 0.1 M $KHCO_3$ solution was 3.44 μmol cm^{-2} h^{-1} (cf. the CuO NPs/Cu catalyst, for which the methanol production rate was only 0.67 μmol cm^{-2} h^{-1}). Further, under these conditions the CeO_2 NPs/CuO NPs/Cu catalyst displayed a high Faradaic efficiency for CO_2 reduction to CH_3OH (~ 60%) and excellent stability. These findings are significant for the future development of catalytic systems for CO_2 reduction, demonstrating that a simple catalyst modification (i.e., CeO_2 electrodeposition) can dramatically enhance carrier concentrations and the availability of electrons for PEC reduction of CO_2 to valuable commodity chemicals such as methanol.

Acknowledgements This work was financially supported by the National Natural Science Foundation of China (21802089); Natural Science Foundation of Shandong Province (ZR2019BB015); The Science and Technology Plan of Shandong Province Colleges and Universities under Grant (No. J14LC16) and the Natural Science Foundation of Shandong Province under Grant (No. ZR2017MB018). GINW acknowledges funding support from the Shandong Province Double Hundred Talents Program for Foreign Experts, the Energy Education Trust of New Zealand, the Dodd Walls Centre for Photonic and Quantum Technologies, and the MacDiarmid Institute for Advanced Materials and Nanotechnology.

Electronic supplementary material The online version of this article (https://doi.org/10.1007/s40820-019-0354-1) contains supplementary material, which is available to authorized users.

References

1. M. Burke, S.M. Hsiang, E. Miguel, Global non-linear effect of temperature on economic production. Nature **527**, 235–239 (2015). https://doi.org/10.1038/nature15725
2. S. Zhao, S. Li, T. Guo, S. Zhang, J. Wang, Y. Wu, Y. Chen, Advances in Sn-based catalysts for electrochemical CO_2 reduction. Nano-Micro Lett. **11**, 62 (2019). https://doi.org/10.1007/s40820-019-0293-x
3. E.M. Volodin, Relation between temperature sensitivity to doubled carbon dioxide and the distribution of clouds in current climate models. Izvestiya Atmos. Ocean. Phys. **44**, 288–299 (2008). https://doi.org/10.1134/S0001433808030043
4. I. Tan, T. Storelvmo, M.D. Zelinka, Observational constraints on mixed-phase clouds imply higher climate sensitivity. Science **352**, 224–227 (2016). https://doi.org/10.1126/science.aad5300
5. I.C. Prentice, G. Farquhar, M. Fasham, M. Goulden, M. Heimann et al., The carbon cycle and atmospheric carbon dioxide. In IPCC Climate Change2001 (2001), pp. 183–237. http://oceanrep.geomar.de/id/eprint/3422
6. D. Schimel, B.B. Stephens, J.B. Fisher, Effect of increasing CO_2 on the terrestrial carbon cycle. Proc. Natl. Acad. Sci. **112**, 436–441 (2015). https://doi.org/10.1073/pnas.1407302112
7. W. Wang, S. Wang, X. Ma, J. Gong, Recent advances in catalytic hydrogenation of carbon dioxide. Chem. Soc. Rev. **40**, 3703–3727 (2011). https://doi.org/10.1039/C1CS15008A
8. R. Tanaka, M. Yamashita, K. Nozaki, Catalytic hydrogenation of carbon dioxide using Ir(III)-pincer complexes. J. Am. Chem. Soc. **131**, 14168–14169 (2009). https://doi.org/10.1021/ja903574e
9. R. Kuriki, K. Sekizawa, O. Ishitani, K. Maeda, Visible-light-driven CO_2 reduction with carbon nitride: Enhancing the activity of ruthenium catalysts. Angew. Chem. Int. Ed. **54**, 2406–2409 (2015). https://doi.org/10.1002/anie.201411170
10. C. Gao, Q. Meng, K. Zhao, H. Yin, D. Wang et al., Co_3O_4 Hexagonal platelets with controllable facets enabling highly efficient visible-light photocatalytic reduction of CO_2. Adv. Mater. **28**, 6485–6490 (2016). https://doi.org/10.1002/adma.201601387
11. D. Gao, H. Zhou, J. Wang, S. Miao, F. Yang, G. Wang, J. Wang, X. Bao, Size-dependent electrocatalytic reduction of CO_2 over Pd nanoparticles. J. Am. Chem. Soc. **137**, 4288–4291 (2015). https://doi.org/10.1021/jacs.5b00046
12. M. Fujihira, Y. Hirata, K. Suga, Electrocatalytic reduction of CO_2 by nickel(II) cyclam: Study of the reduction mechanism on mercury by cyclic voltammetry, polarography and electrocapillarity. J. Electroanal. Chem. **292**, 199–215 (1990). https://doi.org/10.1016/0022-0728(90)87336-I
13. P. Li, J. Xu, H. Jing, C. Wu, H. Peng, J. Lu, H. Yin, Wedged N-doped CuO with more negative conductive band and lower overpotential for high efficiency photoelectric converting CO_2 to methanol. Appl. Catal. B Environ. **156**, 134–140 (2014). https://doi.org/10.1016/j.apcatb.2014.03.011
14. W.H. Wang, Y. Himeda, J.T. Muckerman, G.F. Manbeck, E. Fujita, CO_2 hydrogenation to formate and methanol as an alternative to photo—and electrochemical CO_2 reduction. Chem. Rev. **115**, 12936–12973 (2015). https://doi.org/10.1021/acs.chemrev.5b00197
15. M. Packer, Algal capture of carbon dioxide; biomass generation as a tool for greenhouse gas mitigation with reference to New Zealand energy strategy and policy. Energy Policy **37**, 3428–3437 (2009). https://doi.org/10.1016/j.enpol.2008.12.025
16. S.R. Chae, E.J. Hwang, H.S. Shin, Single cell protein production of Euglena gracilis and carbon dioxide fixation in an innovative photo-bioreactor. Bioresource Technol. **97**, 322–329 (2006). https://doi.org/10.1016/j.biortech.2005.02.037
17. X. Chang, T. Wang, J. Gong, CO_2 photo-reduction: Insights into CO_2 activation and reaction on surfaces of photocatalysts. Energy Environ. Sci. **9**, 2177–2196 (2016). https://doi.org/10.1039/C6EE00383D
18. L. Jia, X. Sun, Y. Jiang, S. Yu, C. Wang, A novel $MoSe_2$-reduced graphene oxide/polyimide composite film for applications in electrocatalysis and photoelectrocatalysis

hydrogen evolution. Adv. Funct. Mater. **25**, 1814–1820 (2015). https://doi.org/10.1002/adfm.201401814

19. Q. Zhang, L. Gao, J. Guo, Effects of calcination on the photocatalytic properties of nanosized TiO_2 powders prepared by $TiCl_4$ hydrolysis. Appl. Catal. B Environ. **26**, 207–215 (2000). https://doi.org/10.1016/S0926-3373(00)00122-3
20. J. Bisquert, F. Fabregat-Santiago, I. Mora-Seró, G. Garcia-Belmonte, E.M. Barea, E. Palomares, A review of recent results on electrochemical determination of the density of electronic states of nanostructured metal-oxide semiconductors and organic hole conductors. Inorg. Chim. Acta **361**, 684–698 (2008). https://doi.org/10.1016/j.ica.2007.05.032
21. H. Shi, G. Chen, C. Zhang, Z. Zou, Polymeric g-C_3N_4 coupled with $NaNbO_3$ nanowires toward enhanced photocatalytic reduction of CO_2 into renewable fuel. ACS Inorg. Chim. Acta **4**, 3637–3643 (2014). https://doi.org/10.1021/cs500848f
22. S. Zhang, P. Kang, S. Ubnoske, M.K. Brennaman, N. Song, R.L. House, J.T. Glass, T.J. Meyer, Polyethylenimine-enhanced electrocatalytic reduction of CO_2 to formate at nitrogen-doped carbon nanomaterials. J. Am. Chem. Soc. **136**, 7845–7848 (2014). https://doi.org/10.1021/ja5031529
23. Y. Yamazaki, H. Takeda, O. Ishitani, Photocatalytic reduction of CO_2 using metal complexes. J. Photochem. Photobiol. C **25**, 106–137 (2015). https://doi.org/10.1016/j.jphotochemrev.2015.09.001
24. Y. Hori, H. Wakebe, T. Tsukamoto, O. Koga, Electrocatalytic process of CO selectivity in electrochemical reduction of CO_2 at metal electrodes in aqueous media. Electrochim. Acta **39**, 1833–1839 (1994). https://doi.org/10.1016/0013-4686(94)85172-7
25. J. Zhang, S.Z. Qiao, L. Qi, J. Yu, Fabrication of NiS modified CdS nanorod p-n junction photocatalysts with enhanced visible-light photocatalytic H_2-production activity. Phys. Chem. Chem. Phys. **15**, 12088–12094 (2013). https://doi.org/10.1039/C3CP50734C
26. A.J. Cowan, J.R. Durrant, Long-lived charge separated states in nanostructured semiconductor photoelectrodes for the production of solar fuels. Chem. Soc. Rev. **42**, 2281–2293 (2013). https://doi.org/10.1039/C2CS35305A
27. J. Qiao, M. Fan, Y. Fu, Z. Bai, C. Ma, Y. Liu, X.D. Zhou, Highly-active copper oxide/copper electrocatalysts induced from hierarchical copper oxide nanospheres for carbon dioxide reduction reaction. Electrochim. Acta **153**, 559–565 (2015). https://doi.org/10.1016/j.electacta.2014.09.147
28. M. Le, M. Ren, Z. Zhang, P.T. Sprunger, R.L. Kurtz, J.C. Flake, Electrochemical reduction of CO_2 to CH_3OH at copper oxide surfaces. J. Electrochem. Soc. **158**, E45–E49 (2011). https://doi.org/10.1149/1.3561636
29. R. Gusain, P. Kumar, O.P. Sharma, S.L. Jain, O.P. Khatri, Reduced graphene oxide-CuO nanocomposites for photocatalytic conversion of CO_2 into methanol under visible light irradiation. Appl. Catal. B Environ. **181**, 352–362 (2016). https://doi.org/10.1016/j.apcatb.2015.08.012
30. H.R. Kim, A. Razzaq, C.A. Grimes, S.I. In, Heterojunction p-n-p Cu_2O/S-TiO_2/CuO: Synthesis and application to photocatalytic conversion of CO_2 to methane. J. CO2 Util. **20**, 91–96 (2017). https://doi.org/10.1016/j.jcou.2017.05.008
31. P.V. Kamat, Manipulation of Charge Transfer Across Semiconductor Interface. A criterion that cannot be ignored in photocatalyst design. J. Phys. Chem. Lett. **3**, 663–672 (2012). https://doi.org/10.1021/jz201629p
32. S. Qin, F. Xin, Y. Liu, X. Yin, W. Ma, Photocatalytic reduction of CO_2 in methanol to methyl formate over CuO-TiO_2 composite catalysts. J. Colloid Interf. Sci. **356**, 257–261 (2011). https://doi.org/10.1016/j.jcis.2010.12.034
33. H. Kominami, A. Tanaka, K. Hashimoto, Mineralization of organic acids in aqueous suspensions of gold nanoparticles supported on cerium(IV) oxide powder under visible light irradiation. Chem. Commun. **46**, 1287–1289 (2010). https://doi.org/10.1039/B919598J
34. P. Ji, J. Zhang, F. Chen, M. Anpo, Study of adsorption and degradation of acid orange 7 on the surface of CeO_2 under visible light irradiation. Appl. Catal. B Environ. **85**, 148–154 (2009). https://doi.org/10.1016/j.apcatb.2008.07.004
35. J. Graciani, K. Mudiyanselage, F. Xu, A.E. Baber, J. Evans et al., Highly active copper-ceria and copper-ceria-titania catalysts for methanol synthesis from CO_2. Science **345**, 546–550 (2014). https://doi.org/10.1126/science.1253057
36. M.J. Wolf, J. Kullgren, P. Broqvist, K. Hermansson, Fluorine impurities at CeO_2(111): Effects on oxygen vacancy formation, molecular adsorption, and surface re-oxidation. J. Chem. Phys. **146**, 044703 (2017). https://doi.org/10.1063/1.4973239
37. X.H. Lu, D.Z. Zheng, J.Y. Gan, Z.Q. Liu, C.I. Liang, P. Liu, Y.X. Tong, Porous CeO_2 nanowires/nanowire arrays: Electrochemical synthesis and application in water treatment. J. Mater. Chem. **20**, 7118–7122 (2010). https://doi.org/10.1039/C0JM00487A
38. P. Li, H. Wang, J. Xu, H. Jing, J. Zhang, H. Han, F. Lu, Reduction of CO_2 to low carbon alcohols on CuO FCs/Fe_2O_3 NTs catalyst with photoelectric dual catalytic interfaces. Nanoscale **5**(23), 11748–11754 (2013). https://doi.org/10.1039/C3NR03352J
39. L. Artiglia, F. Orlando, K. Roy, R. Kopelent, O. Safonova, M. Nachtegaal, T. Huthwelker, J.A. van Bokhoven, Introducing time resolution to detect Ce^{3+} catalytically active sites at the Pt/CeO_2 interface through ambient pressure X-ray photoelectron spectroscopy. J. Phys. Chem. Lett. **8**, 102–108 (2017). https://doi.org/10.1021/acs.jpclett.6b02314
40. Y. Wang, Z. Chen, P. Han, Y. Du, Z. Gu, X. Xu, G. Zheng, Single-atomic Cu with multiple oxygen vacancies on ceria for electrocatalytic CO_2 reduction to CH_4. ACS Catal. **8**, 7113–7119 (2018). https://doi.org/10.1021/acscatal.8b01014
41. E. Johnson, R. Willardson, A. Beer, Semiconductors and semimetals. Opt. Prop. III-V. Comp. **3**, 153 (1967)
42. K. Gelderman, L. Lee, S.W. Donne, Flat-band potential of a semiconductor: Using the Mott–Schottky equation. J. Chem. Educ. **84**, 685 (2007). https://doi.org/10.1021/ed084p685
43. Z. Yang, J. Xu, C. Wu, H. Jing, P. Li, H. Yin, New insight into photoelectric converting CO_2 to CH_3OH on the one-dimensional ribbon CoPc enhanced Fe_2O_3 NTs. Appl. Catal.

B Environ. **156**, 249–256 (2014). https://doi.org/10.1016/j.apcatb.2014.03.012

44. W. Schottky, Zur halbleitertheorie der sperrschicht- und spitzengleichrichter. Z. Phys. **113**, 367–414 (1939). https://doi.org/10.1007/BF01340116
45. W. Schottky, Halbleitertheorie der sperrschicht. Naturwissenschaften **26**, 843 (1938). https://doi.org/10.1007/BF01774216
46. N.F. Mott, The theory of crystal rectifiers. Proc. R. Soc. Lond. A **171**, 27–38 (1939). https://doi.org/10.1098/rspa.1939.0051
47. P. Li, X. Sui, J. Xu, H. Jing, C. Wu, H. Peng, J. Lu, H. Yin, Worm-like InP/TiO_2 NTs heterojunction with unmatched energy band photo-enhanced electrocatalytic reduction of CO_2 to methanol. Chem. Eng. J. **247**, 25–32 (2014). https://doi.org/10.1016/j.cej.2014.03.001
48. P. Burroughs, A. Hamnett, A.F. Orchard, G. Thornton, Satellite structure in the X-ray photoelectron spectra of some binary and mixed oxides of lanthanum and cerium. J. Chem. Soc. Dalton Trans. **17**, 1686–1698 (1976). https://doi.org/10.1039/DT9760001686
49. C. Ho, J.C. Yu, T. Kwong, A.C. Mak, S. Lai, Morphology-controllable synthesis of mesoporous CeO_2 nano—and microstructures. Chem. Mater. **17**, 4514–4522 (2005). https://doi.org/10.1021/cm0507967
50. S. Issarapanacheewin, K. Wetchakun, S. Phanichphant, W. Kangwansupamonkon, N. Wetchakun, A novel CeO_2/Bi_2WO_6 composite with highly enhanced photocatalytic activity. Mater. Lett. **156**, 28–31 (2015). https://doi.org/10.1016/j.matlet.2015.04.139